

PAPER

Pockets, jumps and filaments: classifying ionic motion and determining the role of structure in electrochemical properties of $2\text{Li}_2\text{S-GeS}_2$ superionic glasses

To cite this article: Matthieu Micoulaut 2024 *J. Phys.: Condens. Matter* **36** 195703

View the [article online](#) for updates and enhancements.

You may also like

- [Absolute calibration of the ratio of Xe/O two-photon absorption cross-sections for O-TALIF applications](#)
Zhan Shu, Nikolay A Popov and Svetlana M Starikovskaia
- [The Electrochemical Reaction of Zinc Oxide Thin Films with Lithium](#)
Zheng-Wen Fu, Feng Huang, Ye Zhang et al.
- [Thermal transport in Yb-based 1-2-20 materials](#)
Chinedu E. Ekuma



**EDINBURGH
INSTRUMENTS**

WORLD LEADING
MOLECULAR
SPECTROSCOPY SOLUTIONS

edinst.com

The advertisement features a red background with the Edinburgh Instruments logo on the left, which consists of a stylized sunburst of white dots. In the center and right, several pieces of laboratory equipment are displayed, including a large white and black spectrometer labeled 'FLS 1000' and a smaller instrument labeled 'FSS'. The text 'WORLD LEADING MOLECULAR SPECTROSCOPY SOLUTIONS' is written in white, bold, sans-serif font on the left side. The website 'edinst.com' is shown in a white box on the bottom right.

Pockets, jumps and filaments: classifying ionic motion and determining the role of structure in electrochemical properties of $2\text{Li}_2\text{S-GeS}_2$ superionic glasses

Matthieu Micoulaut 

Sorbonne Université, Laboratoire de Physique Théorique de la Matière Condensée, CNRS UMR 7600, 4 Place Jussieu, 75252 Paris Cedex 05, France

E-mail: mimi@lptl.jussieu.fr

Received 18 October 2023, revised 22 December 2023

Accepted for publication 5 February 2024

Published 14 February 2024



Abstract

The structural properties of a typical solid electrolyte system ($2\text{Li}_2\text{S-GeS}_2$) is investigated from First principles molecular dynamics simulations. Results reveal that depolymerization of the base GeS_2 network by alkali additives takes place but appears reduced with respect to the corresponding sodium analog glass. Experimental structure functions are reproduced and reveal that the network is dominated by $\text{GeS}_{4/2}$ tetrahedra that are connected by edges (four-membered rings) and corners and disrupted by the addition of lithium, albeit a non-negligible fraction of connecting tetrahedra (Q^2 units) are still present in the glass structure. Dynamic and electric properties are also studied and emphasize that the size of the migrating cation (Li) is essential for ensuring a good level of ionic conductivity as it displays increased values with respect to the parent Na-bearing system. On the atomic (picosecond) timescale, different typical Li trajectories are identified and their distribution calculated: reduced cage-like motion in pockets constrained by the surrounding (Ge,S) network, back and forth jump motions with short transition states and long-range filamentary motion.

Supplementary material for this article is available [online](#)

Keywords: glasses, solid electrolytes, molecular dynamics, chalcogenides

1. Introduction

With the increase of mobile applications, the need of improved and more safer electrochemical energy storage devices has become a crucial topic in our society. Among various technologies, fast ion batteries (e.g. Li-ion batteries, LiB) have led to a wide range of applications in mobile phones, electric bikes, scooters, and larger vehicles [1, 2]. These LiBs usually contain a Li-based oxide cathode (e.g. LiCoO_3) together with a liquid electrolyte that ensures conduction during charge

and discharge cycling. However, such devices are subjected to safety hazard because of the presence of flammable organic flour-containing solvents in the electrolytes. It has also been shown that the dendritic growth of Li filaments can lead to shortcuts and possible explosive batteries.

Solid state batteries, thus, represent an interesting and safe alternative to the present LiBs [3], and glasses acting as solid electrolytes have been identified as promising materials in this respect [4] because one is able to optimize their electrochemical properties by extending the range in

composition or by alloying into base glasses a certain number of additives to increase stability and conductivity [5]. Among glasses, sulfides have been found to display the largest conductivities and can be formed over extended domains in composition such as $\text{Li}_2\text{S}-\text{P}_2\text{S}_5$ which have now motivated a large number of studies due to their important conductivity [6–9], typically $10^{-3} \Omega^{-1}\cdot\text{cm}^{-1}$. Among other possibilities, modified Group IV sulfide network formers (GeS_2 , SiS_2) also represent promising possibilities because of the same level in conduction [10, 11] (for a review, see [12]). Recent studies have for example focused on binary $\text{Li}_2\text{S}-\text{SiS}_2$ glasses [13–15] which have provided an additional insight to early studies performed in the 1980's and 1990's [5, 16–18]. In order to improve the knowledge of parameters influencing ion conduction, it is desirable to increase the knowledge on structure of these systems which have clearly received much less attention than their oxide counterparts.

In the present contribution, we focus on a system, $\text{GeS}_2-2\text{Li}_2\text{S}$, which appears to be also an interesting candidate for solid state LiBs, and the network former GeS_2 has furthermore been used as an additive in different sulfide electrolytes (mixed network former effect). Such lithium thiogermanates have been studied by different techniques. The pioneering work is due to Ribes, Pradel and co-workers [19–22] who produced $(100-x)\text{GeS}_2-x\text{Li}_2\text{S}$ over the range $30 \leq x \leq 50\%$, and subsequently analyzed the structural, spectroscopic and electric properties of the corresponding glasses, including mixed network-former effects [23, 24]. Conductivity values were of about $4 \times 10^{-2} \text{ mS}\cdot\text{cm}^{-1}$ at room temperature, as also confirmed independently by other authors [25]. This level of conductivity makes the present Li-based thiogermanate glasses very attractive for possible applications, and recent measurements on multicomponent electrolytes have suggested, indeed, that the $\text{Li}_2\text{S}-\text{GeS}_2$ system can be used as base material for a massive improvement of Li-ion conductivity [26, 27]. More recently, neutron and x-ray diffraction (XRD) studies have been performed over almost the same range of composition in these thiogermanate glasses [28–30], and they have permitted to validate three-dimensional structure models by using Reverse Monte Carlo [31] (RMC) and molecular dynamics (MD) simulation techniques [29] at low temperature where activation barriers for structural relaxation are notoriously large. Such models reveal that the base network features (i.e. GeS_2) are still present at low Li content such as edge-sharing tetrahedra, and the Li ions are essentially located in a deformed octahedral site. The short-range order (SRO) of such glasses and its modification with alkali addition are similar to many other modified tetrahedral networks (silicates, thiosilicates) [32, 33]. The base GeS_2 network consists in corner- and edge-sharing tetrahedra [34, 35], and these are usually termed as Q^4 units since each Ge atom has four so-called ‘bridging sulfurs’ (BS) connecting the tetrahedra to each other. Upon Li addition, the network is disrupted and more and more Li ions appear in the vicinity of the sulfur atoms. As a result of the depolymerization, the number of sulfur atoms connecting two $\text{GeS}_{4/2}$ tetrahedra together decreases, and different Q^n species with $n < 4$ appear upon Li content increase (figure 1). Here n represents

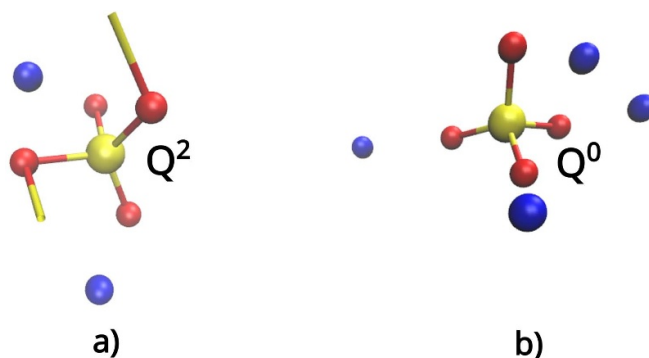


Figure 1. A selection of possible tetrahedra (Q^n species) in L2G glasses : (a) a Q^2 unit having two BS and two NBS atoms. (b) a Q^0 unit having only NBS atoms. See calculated statistics given below. Ge, S and Li atoms are colored yellow, red and blue, respectively.

the number of BS atoms. These additional units contain $4-n$ ‘non-bridging sulfur’ (NBS) atoms and have as nearest neighbors a Ge and a Li atom. This Q^n terminology is rather useful since spectroscopic signatures (Nuclear Magnetic resonance (NMR), Raman spectroscopy [32, 36, 37]) differ with various n values so that the Q^n speciation and the SRO can be experimentally characterized as a function of modifier content or even thermodynamic conditions.

As previously emphasized [29, 31], computational techniques permit to calculate properties and to establish relationships between the structure at the atomic scale with ensemble averaged quantities of interest such as diffusion or conductivity. While the modeling has been essentially based on a classical [29] or phenomenological basis [31], here we investigate the structural and electrochemical properties of a archetypal thiogermanate, namely $2\text{Li}_2\text{S}-\text{GeS}_2$ (L2G), from a density functional theory (DFT) based MD simulation. The choice of the composition is motivated by the importance of the obtained large conductivities at large Li content, and by the fact that a corresponding Na analog (i.e. N2G) has been studied recently [38]. The use of DFT is motivated by the fact that the charge transfer involved in the covalent bonds imposes an explicit treatment of the chemical bonding. One has, therefore to account for electronic interactions that are missed by classical treatments which, furthermore, are known to reproduce only fairly the structural properties of chalcogenides [39] among which, bonding defects [40] leading to broken chemical order. Germanium Sulfides and Selenides display, indeed, a certain number of homopolar defects such as S–S, Se–Se, Ge–Ge or As–As in the stoichiometric compounds such as GeS_2 [34], GeSe_2 [41] or As_2Se_3 [42]. These defects have been revealed from neutron diffraction using isotopic substitution which delivers difference functions in which atomic correlations (e.g. Ge–Ge, Ge–S, etc) can be eliminated and lead to a full account of the partial pair correlations, i.e. Ge–Ge, Ge–S and S–S correlations in real and reciprocal space. The breakdown of chemical ordering in chalcogenide network formers cannot be described from classical force-fields (e.g. Buckingham potentials) which lead in most if not all situations to a nearly 100% heteropolar network (silica-like). We are not

aware of any classical potential for L2G, and the one proposed in [29] is based on an artificially partial frozen Ge-S network with interaction parameters provided only for the Li atoms.

Our results show a rather correct agreement in reciprocal space for a x-ray measured structure function (structure factor) of a slightly different composition (LG), whereas the real space functions exhibit an excellent agreement with experiments and consists in a principal peak corresponding to the Ge-S bond distance and a secondary peak associated with Ge-Ge and S-S correlations. While the coordinations are somehow expected ($r_{Ge} = 4$, $r_S = 2$ and $r_{Li} = 3.5$, the latter in defect octahedral geometry), the statistics of Q^n species suggests a network with a remaining (Ge,S) connectivity as a non-zero fraction of Q^2 (and a subsequent meaningful ring statistics) with two bridging sulfur (BS) atoms is found. In contrast to oxides however, there is an obvious presence of homopolar Ge-Ge bonds, - a feature typical of Ge chalcogenides [35, 41–44] -, and these induce in L2G the presence of isolated $Ge_2S_6^{6\ominus}$ anions. The dynamics of the supercooled liquids (diffusivity) suggests an Arrhenius behavior with temperature, and the calculated values appear to be compatible with tracer diffusion experiments obtained for other chalcogenide electrolytes [45–47]. The Li motion appears to be complex and heterogeneous in character, and on the 1-10 picosecond timescale manifests by at least three categories of ions evolving either in spatially reduced cages (pockets), jumping between neighboring sites or following filamentary pathways. Similar conclusions can be drawn when the calculated conductivity $\sigma(T)$ is compared to experiments and the important carrier mobility appears to be driven by the filamentary Li motions that already take place on short timescales.

2. Methods

The DFT MD based simulations (Car-Parrinello scheme [48, 49] with the CPMD code) have been performed on a system containing $N = 300$ atoms with $N_S = N_{Li} = 132$ and $N_{Ge} = 36$ (see supplementary information). A periodically repeated cubic cell has been used, with edges L satisfying the experimental number density ρ_0 of the corresponding glasses [29], i.e. $L = 17.91 \text{ \AA}$. DFT in combination with plane wave basis sets was used, the electronic scheme being based on a Perdew-Burke-Ernzerhoff (PBE) functional within a generalized gradient approximation (GGA) for the exchange correlation energy [50]. The electronic structure of the liquids and glasses was described within DFT and evolved self-consistently during the motion with valence electrons being treated explicitly, in conjunction with norm-conserving pseudopotentials to account for core-valence interactions. The wave functions were expanded at the Γ -point of the supercell and the energy cutoff was set at 80 Ry.

The starting configuration was used from an isochemical compound $2Na_2S-GeS_2$ studied previously [38], and Na were replaced by Li atoms with an appropriate rescaling of the simulation box, i.e. the fractional coordinates of the N2G glass have been used, and the cell length has been decreased from 19.26

(cell length of N2G) to 17.91 \AA . After a loss of the memory of the initial configuration achieved through preliminary runs at 2000 K over 10 ps with a timestep of $\Delta t = 0.12 \text{ fs}$ and a fictitious mass for the electron of 2000 a.u., the system was maintained at different target temperatures, 1200 K, 900 K and 600 K, each accumulated over 15 ps, and finally 300 K for 20 ps. The cooling procedure was performed in a sequential fashion, e.g. the equilibration at 900 K started from the last configuration (positions/velocities) obtained at 1200 K, and so on. The presented results at 300 K and the liquid temperatures are obtained from a statistical average over 12 ps, once the first 3 ps have been discarded.

3. Results on structure

3.1. Comparison of structure functions

In figure 2(a) are represented the measured [29] and calculated x-ray total structure factors $S(k)$. Note that the measured composition slightly differs (i.e. LG) from the simulated one (L2G) as we are not aware of any scattering study on the L2G composition. Here, the total weighted structure factors are derived using the partial correlations $S_{nm}(k)$

$$S(k) = \langle f \rangle^{-2} \sum_{n,m} c_n c_m f_n f_m S_{nm}(k) \quad (1)$$

with:

$$\langle f \rangle = \sum_n c_n f_n = c_{Ge} f_{Ge} + c_S f_S + c_{Li} f_{Li} \quad (2)$$

where the f_n represent the atomic form factors ($f_{Ge} = 32$, $f_S = 16$, $f_{Li} = 3$), and c_n represent the species concentration, respectively. The partial correlations in Fourier space have been evaluated either directly from the atomic positions which permit to extract the total structure factor $S(k)$ using equation (1) (gray curve, figure 2(a)),

$$S_{nm}(k) = \frac{1}{N} \left\langle \sum_n \sum_m e^{-ik \cdot (\mathbf{R}_n - \mathbf{R}_m)} \right\rangle \quad (3)$$

or from a Fourier transform (black curves, figure 2(a)) of the partial pair correlation functions $g_{nm}(r)$:

$$S_{nm}(k) = 1 + \rho_0 \int_0^\infty 4\pi r^2 [g_{nm}(r) - 1] \frac{\sin(kr)}{kr} dr \quad (4)$$

where ρ_0 is the system density. One recovers here the principal peak positions and amplitudes of the measured total structure factor, although the low momentum region ($k < 2.5 \text{ \AA}^{-1}$) exhibits a more fair reproduction with the contrast between the first sharp diffraction peak (FSDP at 1.1 \AA^{-1}) and a neighboring peak at $k_2 = 2.0 \text{ \AA}^{-1}$ being obviously underestimated from the simulation. In addition, the position of the FSDP is overestimated (1.25 \AA^{-1} versus $k_{FSDP} = 1.10 \text{ \AA}^{-1}$ [29]) while the opposite trend is obtained for the second peak (1.98 \AA^{-1} versus $k_2 = 2.11 \text{ \AA}^{-1}$). There might clearly be some effects

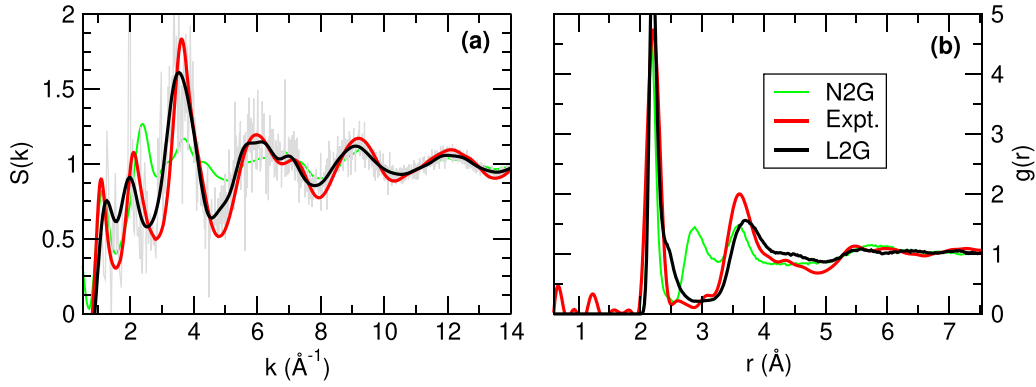


Figure 2. Calculated (black) total structure factor $S(k)$ (a) and pair correlation functions $g(r)$ (b) of L2G glasses. For comparison, XRD data from Itoh [29] (red) have been added for the LG composition. The green curve corresponds to calculations from a simulated N2G glass [38].

due to composition since we compare a L2G system with the experimental LG one [29], and it is known that the position k_2 reduces with Li_2S content as it evolves from 2.18 \AA^{-1} in LG4 ($20\text{Li}_2\text{S}-80\text{GeS}_2$) down to 2.11 \AA^{-1} for LG. One also has to keep in mind that the network of a LG glass is still rather polymerized ($Q^2 = 100\%$ in an ideal chemical model or 30% BS atoms from a RMC modelling [29]) so that contributions arising from network-related partials (Ge-S or S-S, see below) of a LG glass in the region $1-3 \text{ \AA}$ might differ substantially from those obtained for the present investigated system. Conversely, the more reasonable agreement at larger k values between simulation and experiment is an indication that the SRO (i.e. tetrahedral) of the network is correctly reproduced and similar between LG and L2G glasses. A recent Gaussian decomposition in Fourier space of structure factors has shown that features beyond the principal peak (PP) region ($k \geq 6 \text{ \AA}^{-1}$) are associated with second-neighbor correlations [51]. The shoulder peak at $\approx 7 \text{ \AA}^{-1}$ is also reproduced from the simulation and provides therefore some confidence that both realistic SRO and second-order correlations are embedded in the DFT structural models.

The decomposition into weighted partials $\langle f \rangle^{-2} f_i f_j c_i c_j S_{ij}(k)$ indicates that the correlations in the scattering function are dominated by the network-forming species, i.e. Ge-S and S-S (figure 3), the presence of a reduced number of Ge atoms in this highly depolymerized glasses leading to a rather small contribution from $S_{\text{GeGe}}(k)$. The remaining partial having a relevant contribution, especially at low k , arises from the Li-S one.

It is interesting to compare the reciprocal structure of the present L2G glass with the corresponding sodium analog that has been recently investigated [38] (green curves in figure 2). One acknowledges that as both Li- and Na- functions $S(k)$ nearly overlap at large k , a similar (tetrahedral) SRO can be anticipated, whereas differences clearly emerge for $k < 6 \text{ \AA}^{-1}$ (i.e. beyond second-shell correlations [51]), which underscore a probable different intermediate range order (IRO) as quantified below.

Real space correlations are represented in figure 2(b) with the calculated and x-ray measured [29] total pair correlation function $g(r)$, together with the analog result for the sodium glass N2G. Again, we note that the main features of the

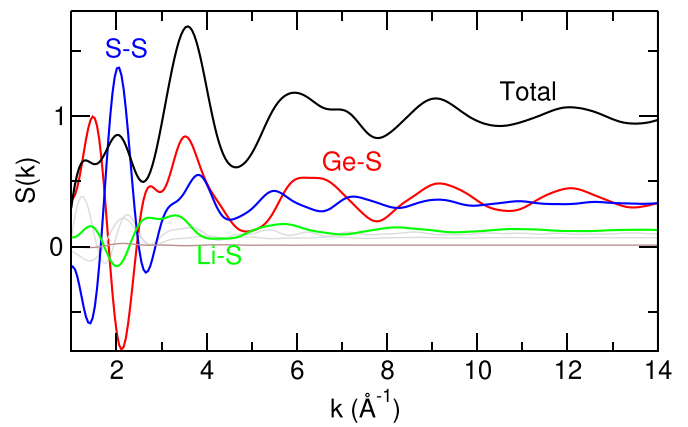


Figure 3. Decomposition of the calculated total structure factor $S(k)$ (black, same as figure 2) into relevant weighted partials (colored curves). The gray curves correspond to partials with a small contribution (Ge-Ge, Ge-Li and Li-Li).

experimental function $g(r)$ are recovered with an excellent reproduction from the simulation of the main peak (amplitude and bond length) at $r \approx 2.36 \text{ \AA}$ which arises from Ge-S correlations (see below). All other features are also reproduced, i.e. the second-shell correlations (S-S) somewhat below 4.0 \AA and a shoulder peak at $r > 4 \text{ \AA}$. The typical peak found at $r \approx 3.0 \text{ \AA}$ in the corresponding N2G glass is not found in the present lithium system as it arises from alkali related correlations that are very small in x-ray weighted functions because of the small form factor of Li ($f_{\text{Li}} = Z_{\text{Li}} = 3$). Indeed, Na-related correlations (essentially Na-S) form an important peak at this distance that is promoted in the total function due an increased form factor ($f_{\text{Na}} = 11$) [38].

3.2. Partial correlations, coordinations and Q^n species

Figure 4 now represents the different atomic partial pair correlation functions which serve for the identification of typical bonding distances (bond lengths, the distances at the principal peaks). We, again, compare the findings with those obtained for N2G, and also with GeS_2 [35]. The presence of an intense peak at 2.24 \AA in the Ge-S partial (figure 4(b)) signals the

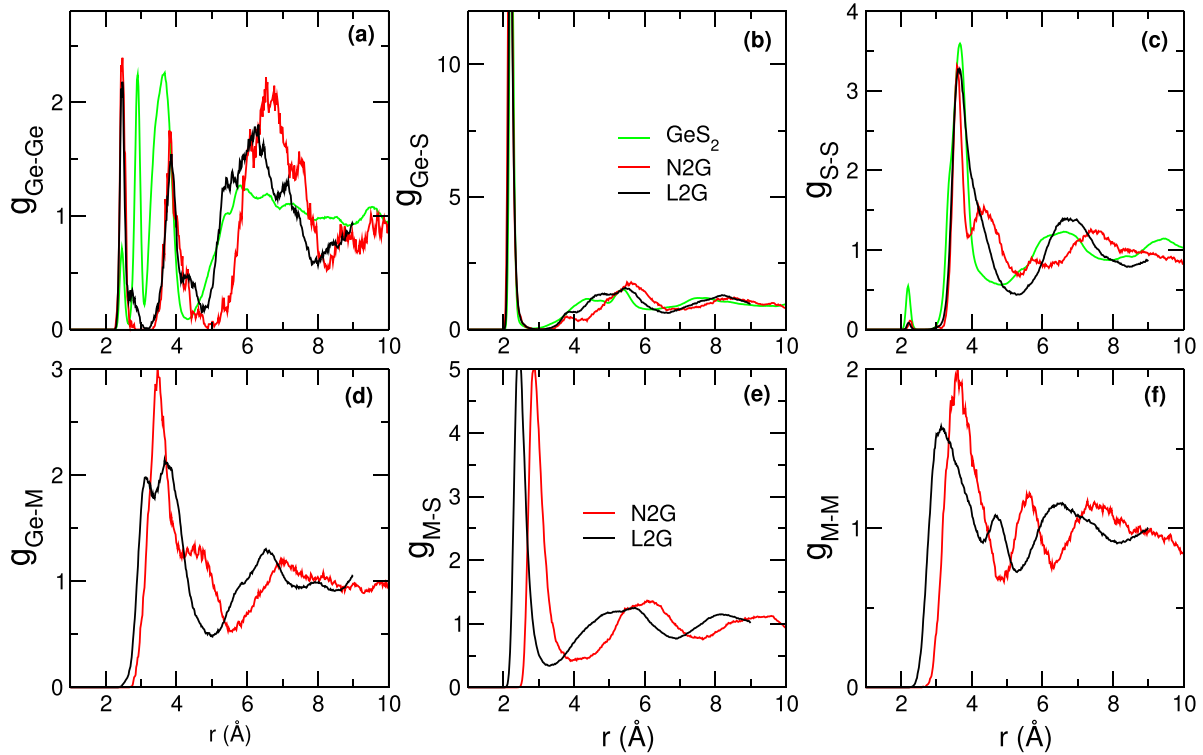


Figure 4. Partial pair correlation functions $g_{ij}(r)$ of LG2 ($M = \text{Li}$, black) and N2G ($M = \text{Na}$, red [38]), together with corresponding partials for amorphous GeS_2 (green [35]).

presence of the Ge–S bond, i.e. the apex of the tetrahedral base geometry whose edges are represented by the S–S bond at 3.61 Å (figure 4(c)). It is easy to check that the tetrahedral ratio $\delta = d_{\text{S-S}}/d_{\text{Ge-S}}$ [52] is equal to 0.620, i.e. close to the value $\sqrt{3}/8 = 0.612$ found for a regular tetrahedron, as in other chalcogenides [53].

The three peak structure of the Ge–Ge partial (figure 4(a)) is typical of Ge chalcogenides and such peaks have been unambiguously assigned [35, 53–55] to homopolar Ge–Ge bonds (2.43 Å), Ge–Ge correlations involved in edge-sharing (ES, 2.91 Å) and corner-sharing tetrahedra (CS, 3.89 Å). In the present L2G system, we note the presence of such motifs, the presence of ES motifs being however much smaller as compared to the base glass GeS_2 [35], and associated with a typical distance (the diagonal of the ES motif corresponding to a Ge–Ge correlation) that is obviously reduced (2.77 Å) with respect to the base GeS_2 (2.88 Å) as it now only forms a shoulder peak on the high r side of the Ge–Ge pre-peak (figure 4(a)). The presence of this typical distance (absent in N2G) suggests that, unlike for the sodium glass, depolymerization of the network is not entirely fulfilled in L2G with ES motifs and IRO being maintained to some extent, as characterized below from the rings statistics.

Other typical distances appear from the inspection of the Li-related partials (figures 4(d)–(f)), and these are also compared with the corresponding Na glass. We first note that the Li–S distance is detected at 2.52 Å, i.e. slightly smaller than the one associated with Na–S (2.88 Å). This obtained Li–S bond distance is consistent with the one determined in Li_2S crystals

[56] (2.47 Å), and involves by definition the NBS atom that connects to a Ge atom (figure 1), and also contributes to the principal peak of the Ge–Li pair correlation function (3.53 Å, figure 4(d)). As emphasized above, such NBS atoms are typical of modified oxides or sulfides, and appear when network glasses are depolymerized by alkali additives. The base glass (e.g. GeS_2) and the bridging sulfur bonds Ge–BS–Ge connecting two tetrahedra together are, indeed, progressively disrupted by alkali ions M , and induce instead a growing presence of Ge–NBS– M bonds.

We furthermore note that that pair correlation functions involving the network-forming species (figures 4(b) and (c)) display a moderate change when one compares GeS_2 with L2S or N2S at short distance. This simply reflects that the typical short distances defining the tetrahedra are maintained, i.e. the Ge–S (2.20 Å) and the S–S distances (3.60 Å).

In figure 5, we represent the bond distance distribution around the Ge atoms, depending on the nature of the S atoms: BS or NBS. An obvious difference emerges, in line with previous findings on NG2 and also thiosulfates [57], and reveals that Ge–NBS bonds are, on average, shorter than Ge–BS ones. One finds, indeed, a Ge–NBS bond distance distribution centered at 2.20 Å whereas it is more likely of about 2.25 Å for Ge–BS bonding distances, i.e. one has an average bond distance difference of about 0.05 Å. Such features have been first detected in corresponding oxide glasses and crystals, e.g. lithium or sodium silicates. Here, a marked difference around the Si atom depending whether the oxygen atom is bridging (BO) or non-bridging (NBO), has been detected in e.g. $\alpha\text{-Na}_2\text{Si}_2\text{O}_5$

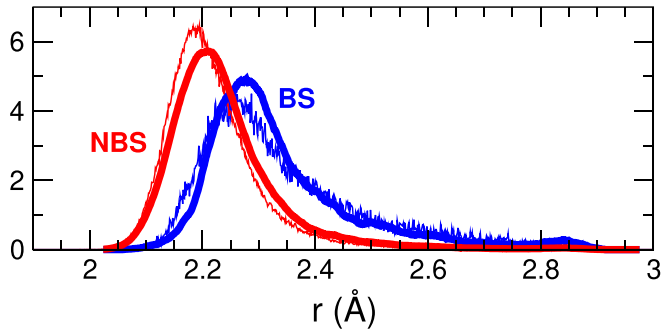


Figure 5. Calculated Ge-BS (blue) and Ge-NBS (red) bond distance distribution in the L2G glass (thick curves), and compared to corresponding results for the N2G glass [38] (thin curves).

and Na_2SiO_3 crystals [58, 59], and have been also calculated in simulated glasses [60, 61] where the bond distance difference is of about 0.08–0.1 Å, i.e. the Si–BO is slightly longer than the Si–NBO bond length.

One, thus, acknowledges that as for e.g. lithium silicates [62] or thiosilicates [57], a bond length difference between the Group IV atom (Si,Ge) and the BS or NBS atoms is found. The physical origin of bridging atom (BO,BS) vs non-bridging atom (NBO,NBS) bond distance difference is obviously common to silicates and thiosilicates, and is linked with the influence of the lithium ions on the neighboring charges and the ionic-covalent character of the bonding that modifies the electronic structure of next neighbor Group IV atoms. The present analysis is in line with the structure analysis of sodium thio-germanate crystals ($\text{Na}_4\text{Ge}_4\text{S}_{10}$) as it was recognized [63] that the Ge–NBS distances are shorter (2.14 Å) than the Ge–BS ones (2.19 Å). In addition, a recent analysis [38] for N2G glasses suggests that the non directional character of the NBS–Na bond induces an electronic density of NBS atoms that points essentially towards the close Ge atom with a rather well defined depletion of the valence charge. This feature obviously contrasts with the characteristics obtained for the BS atoms for which the p orbitals contribute to the deformation of the valence charge in a direction perpendicular to the Ge–Ge line connecting two CS tetrahedra, involving an obvious reduced depletion. Although the electronegativity difference with Li is smaller [64] when compared to oxides ($\Delta\chi_{\text{Li-S}} = 1.60$ and $\Delta\chi_{\text{Li-O}} = 2.46$), one expects to see charge separation (i.e. ionic character) reduced with a possible reduced alteration of the Ge environment but it is certain that the obtained small differences obtained in figure 5 reflect a delicate balance between electron localization on the atomic sites involved in ionic bonding and electronic delocalization, i.e. covalent effects that are more pronounced in sulfur-based glasses.

3.2.1. Coordination numbers. Using the cut-offs of corresponding pair correlation functions $g_{ij}(r)$ (figure 4), we can calculate the coordination number of the different atomic species. For Ge, we find a coordination number $n_{\text{Ge}} = 3.94$ that arises essentially (95%) from of the Ge–S coordinations, the small fraction of homopolar Ge–Ge bonds which lead to the

small pre-peak at 2.43 Å representing the other contribution. The sulfur coordination is found to be $n_{\text{S}} = 2.02$, and essentially linked to two Ge atoms (BS), or to one Ge and a Li atom (NBS). Here, the contribution to the coordination is dominated by Li–S (74.4%) and Ge–S (23.2%). These findings confirm the overall four-fold character of the network made of Ge atoms with coordinations (Ge,S) fulfilling the octet rule.

Finally, the Li coordination is about $n_{\text{Li}} = 3.5$, i.e. slightly larger than the one determined for corresponding lithium thiosilicates using a classical force field [57]. Here, it was found that $n_{\text{Li}} = 2.9$ that was merely consistent with an estimate from neutron scattering [65] ($n_{\text{LiS}} = 3.0$) but somewhat smaller than the value of 4.1 determined independently from scattering data [66] using a rather large Li–S distance (2.7 Å).

3.2.2. Q^n species. In order to characterize the SRO, we use the Q^n terminology which represents the population of Ge tetrahedra having n BS (figure 1). Their population with thermodynamic conditions (pressure, concentration, temperature,...) can usually be directly measured from solid state NMR albeit such measurements are hard to realize in Ge-based glasses in contrast to experiments on (thio)silicates which can utilize a useful isotope (^{29}Si) [12, 17, 67, 68]. As a result, we are only aware of a Raman study [36] of alkali germanates, which also permits by Gaussian deconvolution to access to the Q^n population.

Table 1 provides the Q^n population for the present lithium thio-germanates, which is found to be made of a mixture of Q^2 (13.3%), Q^1 (29.1%) and Q^0 (57.6%) motifs. Given the concentration, the dominant presence of Q^0 is not surprising as a perfect chemical model of L2G would lead to 100% Q^0 , whereas a topological model applied to the parent lithium thiosilicate leads to 100% Q^1 tetrahedra [69]. When compared to the corresponding sodium N2G system [38], obvious differences emerge, and these suggest that for the same amount of alkali modifier the present Li system is more polymerized as the N2G glass does not contain Q^2 species at all. In fact, such species are responsible for the increased network connectivity given their number of BS atoms (figure 1(a)). Our Q^n population furthermore leads to a calculated fraction of NBS that is very large (85.2%), and consistent with an experimental estimate from x-ray photoemission spectroscopy [70] (87.4%) in $2\text{Li}_2\text{S-GeS}_2$, and a RMC modelling [29] of LG (90%).

As a final comment, one should stress that such a characterization is certainly useful as there is a major difficulty in establishing experimentally the Q^n speciation from NMR in sulfide glasses [17]. This is due to the fact that there are only a small number of reference crystalline phases in thio-germanates and thiosilicates [71] (Li_5GeS_6 and Li_4GeS_4 in the Li–Ge–S system) in comparison to corresponding oxides, and these usually serve for the NMR chemical shift identification prior to the glass analysis. Secondly, the small observed chemical shift anisotropies in crystalline thiosilicates do not permit to distinguish between various Q^n geometries. In contrast to lithium silicates [72], the addition of alkali modifiers into SiS_2 leads, indeed, only to small variations in the chemical shift

Table 1. Calculated fraction of Q^n distribution (in%) in L2G glasses, and compared to previous results on the isochemical N2S.

	Q^2	Q^1	Q^0
L2G	13.3	29.1	57.6
N2G [38]		41.1	58.9
Ideal chemical N2G model			100.0

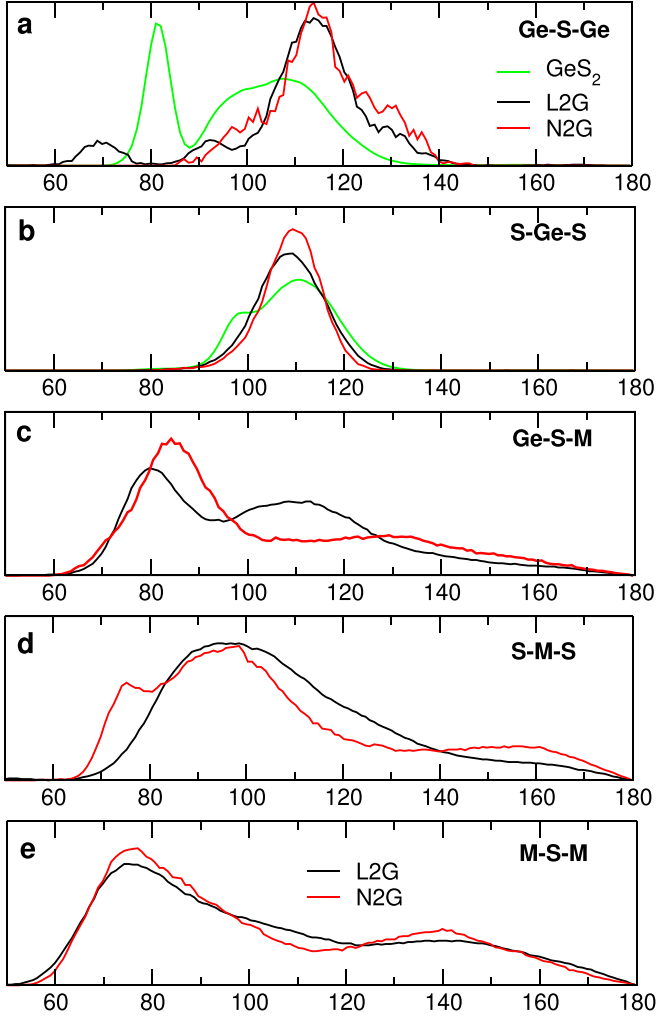


Figure 6. Angles for amorphous L2G (M = Li, black), N2G (M = Na, red [38]) and GeS₂ (green [35]).

[73] so that the Q^n distribution with composition is difficult to establish.

3.3. Bond angles

Figure 6 represents the relevant bond angle distributions (BAD) for the present L2G together with the corresponding sodium glass N2G [38] and the network former [35] for Ge–Se–Ge and S–Ge–S BADs (green curves). The S–Ge–S distribution (figure 6(b)) is found to be close to the BAD obtained for the network former (GeS₂), which signals that the base geometry has not been substantially modified by the Li ions

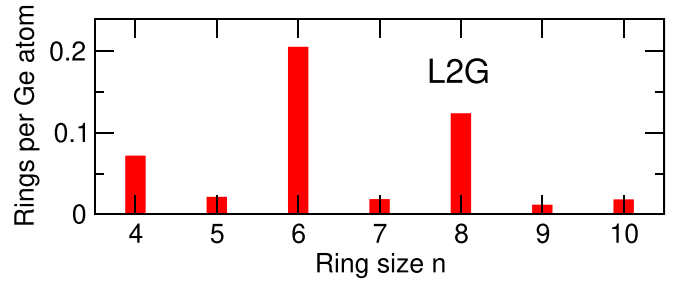


Figure 7. Ring distribution in the present L2S (a) glass.

as it still consists of GeS_{4/2} tetrahedra, its presence being revealed from the dominant peak found at $\arccos(-1/3) = 109.47^\circ$. Conversely, the addition of an alkali modifier leads to a dramatic change of the Ge–S–Ge BAD, whose average angle for GeS₂ (110°) shifts to larger values (average 112°), this being obtained for both lithium and sodium systems. The bimodal distribution in Ge–S–Ge (figure 6(a)) detected [35] in the network former GeS₂ (80° and 105°) is still present but results in L2G from angles that are substantially increased (90° and 115°) and this indicates the presence of both CS and ES-sharing tetrahedra in L2G, the peak at $\simeq 90^\circ$ being associated with the latter while the main peak at $\simeq 115^\circ$ is the signature of BS atoms linking the Ge tetrahedra by corners.

While Ge–S–Li leads to a broad distribution (figure 6(c)), which indicates a variety of environments found for the Li ions in the vicinity of NBS atoms, the S–Li–S BAD signals a possible defect octahedral environment for Li because the BAD S–Li–S profile displays a broad peak centered at $\simeq 90^\circ$ together with a substantial contribution at 180°. We note that there is no fundamental difference with the other BADs when both Na and Li glasses are being compared (figures 6(d) and (e)).

3.4. Ring structure

We have mentioned above that the partial pair correlation functions $g_{GeGe}(r)$ and the total calculated or measured $g(r)$ of the base network GeS₂ [34, 35] contain the signature of ES tetrahedra which represent a $n = 4$ ring. Such IRO elements and also other rings can be characterized from a dedicated analysis. We use a ring statistics algorithm that builds on a rigorous investigation of networks generated using simulation (RINGS) code [74]. Here, the concentration of rings of size $n \leq 10$ (figure 7) are considered with a cutoff (2.80 Å, the minimum of the pair correlations) that permits one to focus only on rings belonging to the network species (Ge,S). The algorithm is mostly based on the King [75]-Franzblau [76] shortest-path search, and statistics over the (Ge,S) network indicates remaining ring structures for the L2G system (figure 7) with dominant contributions from even-sized rings, and especially $n = 4, 6$ and 8. Unlike N2G for which a complete depolymerization of the base network upon important Na addition has been obtained [38], the present L2G systems appears, thus, to maintain a certain degree of IRO. We attribute this difference in behavior by the different size of the alkali atoms, the larger

Na ion being obviously able to disrupt the base network in an increased fashion. The different ring statistics between L2G and N2G also results from the presence of Q^2 species in the former (table 1), which permits to have such rings as several BS atoms are needed to define such structural groupings.

4. Dynamics and conductivity

We now investigate dynamic properties of the L2G system by focusing on the target temperatures in the liquid and supercooled state, any analysis being extracted from the lower temperatures being misleading because of the slowing down of the dynamics that extends beyond the available computer timescale [77].

A first step is the calculation of the mean square displacements (msd) of each atom given by its position $\mathbf{r}_j(t)$ at time t , prior to an appropriate average per species k ($k = \text{Ge, S, Li}$):

$$\langle r_k^2(t) \rangle = \left\langle \frac{1}{N_k} \sum_{j=1}^{N_k} |\mathbf{r}_j(t) - \mathbf{r}_j(0)|^2 \right\rangle \quad (5)$$

where the sum is taken over all atoms of type k .

4.1. Diffusivity

From the calculated mean square displacement $\langle r_k^2(t) \rangle$ of the different species, we calculate the self-diffusion D_k constant in the long-time limit using the Einstein equation:

$$D_k = \frac{1}{6} \lim_{t \rightarrow \infty} \frac{d\langle r_k^2(t) \rangle}{dt}. \quad (6)$$

Note that even for $T = 600$ K, we can safely determine D_{Li} as $\langle r_{Li}^2(t) \rangle$ displays a well-defined diffusive regime that sets in for $t > 5$ ps (not shown). Diffusivity results now appear in figure 8 in an Arrhenius representation, together with data from tracer diffusion measurements (Na, Ag) in the glassy state for similar modified sulfide glasses [45–47]. Given the limited number of simulated data points on L2G (1200 K, 900 K, 600 K), we can hardly comment on the activated (Arrhenius) nature of the Li dynamics but acknowledge a similar trend with inverse temperature when compared to the corresponding sodium system [38], the motion being increased by a factor of about five at 900 K for the Li-system due to obvious alkali size effects, whereas the network species diffusivities appear more reduced as compared to the sodium counterpart.

A estimate of the activation energy assuming an Arrhenius behavior of the form $D_k \propto \exp[-E_A/k_B T]$ leads to $E_A = 0.26(4)$ eV for the Li ions, and to 0.09 eV for the network species, i.e. somewhat smaller than those determined from the parent sodium system (0.33 eV for Na [38]). These data appear consistent with the experimental determination of ion diffusivities [45–47], Li activation barriers for diffusion being obviously smaller when compared to systems with cations of larger size. The results, furthermore, highlight the fact that (i) Na ion dynamics at high temperature is compatible with the one in the glassy state for a parent system (sodium thiosulfate

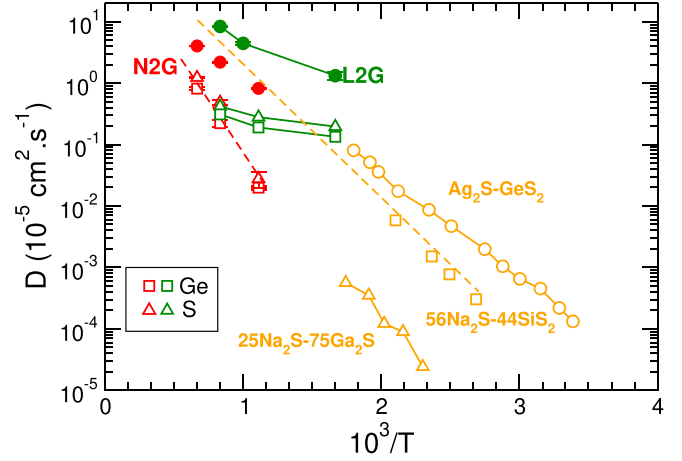


Figure 8. Calculated diffusivity of L2G supercooled liquids (green symbols) as a function of inverse temperature, compared to corresponding data of the sodium analog (N2G [38]): filled circles: Li, open symbols: network species (Ge, S). Data from tracer diffusion measurements of sulfide glasses are also represented (orange open symbols: $\text{Ag}_2\text{S-GeS}_2$ (circles [45]), $25\text{Na}_2\text{S-75 Ga}_2\text{S}_3$ (triangles [46]) and $56\text{Na}_2\text{S-44SiS}_2$ (squares [47])). The broken orange line serves only to highlight the compatibility between calculated Na diffusivity values in the liquid state and experimental values in the glass.

[47], broken orange curve in figure 8), and (ii) Li diffusivities are obviously larger than those found in Ag or Na related systems.

4.2. Jump probabilities

In order to provide some insight into the ion motion and jump probability between anionic sites, we calculate the Van Hove correlation function $G(r, t)$ which is a density-time correlation of particles and permits to quantify correlated real space dynamics [78]. Assume that there is a particle at the origin at time $t = 0$, then the Van Hove correlation for species α (i.e. $\alpha = \text{Li}$) is given by:

$$G(\mathbf{r}, t) = \frac{1}{N_\alpha} \left\langle \sum_{i,j=1}^{N_\alpha} \delta(\mathbf{r} + \mathbf{r}_i(0) - \mathbf{r}_j(t)) \right\rangle \quad (7)$$

where $\langle \cdot \rangle$ denotes the ensemble average, and angular integration reduces the function to the single variable $r = |\mathbf{r}|$ by virtue of the isotropic character of the system. We focus here only on the self part $G_s(r, t)$ the Van Hove correlation function when $i = j$, and which provides some information about hopping mechanisms [77]. Here, $G_s(r, t)$ corresponds to the probability that a Li cation initially at $r = 0$ at time $t = 0$ has jumped by a distance r after a time t .

Figure 9 represents the self-part of the Li Van Hove correlation function $G_s(r, t)$ for different times at 600 K. For short times (almost visible at e.g. 0.01 ps), the function reduces to a Dirac function as expected from its definition (equation (7)). With increasing time, the Li cations can now explore longer distances, and these extend up to 6 Å at 10 ps simulation time

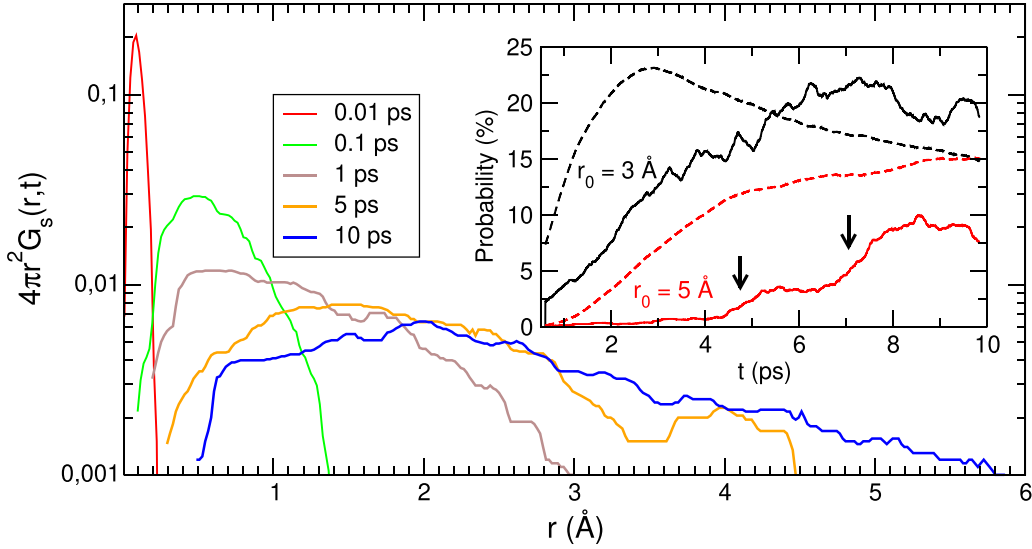


Figure 9. Calculated Li self-part of the Van Hove correlation function $4\pi r^2 G_s(r, t)$ for different times at 600 K in LG2 liquids. The inset shows the calculated jump probability $P(r_0, t)$ represented at fixed r_0 (3.0 Å and 5.0 Å) for $T = 600$ K (solid line), 900 K (broken line).

with average jump distances that increase from 2.6 Å at 600 K to 4.5 Å for 900 K.

Interestingly, the tail of $G_s(r, t)$ at large distance ($r > 3$ Å which is beyond the first coordination shell) is the signature of a departure from a purely Fickian dynamics [79, 80] that is known to lead to the behavior $G_s(r, t) = \exp[-r^2/Dt]$ [78]. This tail is an indication that some cooperative motion is present in the liquid, the feature becoming more pronounced as the viscosity increases close to the glass transition temperature. The trend can be conveniently fitted by a simple exponential [80] $G_s(r, t) \simeq \exp[-r/\lambda(t)]$ with the parameter evolving at 600 K from e.g. $\lambda(t) = 0.66$ Å for $t = 1$ ps to 2.05 Å for $t = 10$ ps. The inspection of the trajectories suggests that the size of the jumps is distributed (see below), and that these arise from cooperative events involving a large number of particles moving by a small amount, similarly to model glass-formers [81], and resulting from possible continuous time random walks of Li cations.

We also consider the probability with time that the particle has jumped by a certain distance (inset of figure 9), i.e. we fix the distance r to some typical jump distance r_0 that merely corresponds to distances between Li sites ($r_0 = 3.0$ Å, figure 4(f)) or to second order Li-NBS correlating distances ($r_0 = 5.0$ Å, figure 4(e)). At low temperature (600 K) when the cation dynamics is limited by the reduced network (Ge,S) motion, the long time limit indicates a near constant jump probability that depends quite naturally on a given jump distance, whereas this is not the case in the high temperature liquid (900 K, broken lines) when network effects are weak because of the larger diffusivity of the (Ge,S) species. In addition, for long-range jumps (5 Å) obvious sudden jump probabilities appear (arrows in the inset of figure 9) and these are found to depend on the time which underscore that the onset of cation motion occurs by steps.

4.3. Classifying moving ions

The motion of such Li ions appears to be complex in character but three generic categories can be sketched on the timescale of interest ($\simeq 10$ ps) from the inspection of the individual msds $r_j^2(t)$ at the temperature close to the glass transition (600 K). These are simply defined by :

$$r_j^2(t) = |\mathbf{r}_j(t) - \mathbf{r}_j(0)|^2. \quad (8)$$

A first category of motion (pocket ions, PIONS) consists in spatially limited motions typical of a cage-like dynamics or vibrations (gray curves b, figure 10) that is constrained by the surrounding network-forming species with a cage size estimated of 50 Å² at 600 K (broken line, figure 10). The calculated average msd corresponding to such identified PIONS is associated with a cage dimension of $\langle R_p \rangle = 4.0$ – 7.0 Å. Secondly, in select situations, the Li ions are able to jump on small distances to a neighboring NBS anionic site before eventually moving back to the initial (or close) NBS site as acknowledged by the msd value close to zero at long times (red curve a, figure 10). This back and forth motion defines a second category of Li motion: back and forth ions (BAFIONS) that also involve spatial extensions of typically 7.0 – 8.0 Å. The third category of Li dynamics corresponds to filamentary motions with a limited time ($\simeq 6$ ps) spent in reduced pockets (filamentary ions (FIONS), blue curve in figure 10(c)) separated by substantial spatial jumps (e.g. at 1 ps and 8 ps, blue curve at figure 10(c)), and leading ultimately to a rather important mean-square displacement (220 Å² at the largest time). Over the simulated time, the statistics of PIONS, BAFIONS and FIONS is $36.6 \pm 1.2\%$, $23.1 \pm 3.1\%$, and $40.3 \pm 4.3\%$, respectively. One, thus, realizes that on the timescale of the simulation the ionic motion is not induced by all carriers as about 36.6% Li ions display a spatially reduced cage-like trajectory. We finally note that the data also indicate that the time

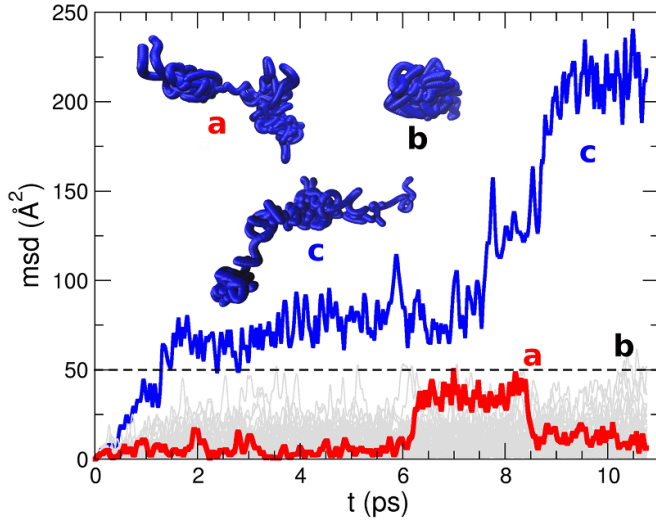


Figure 10. Individual mean square displacements of three select Li ions in 600 K L2G supercooled liquids with typical ionic motions represented by accumulated snapshots: (a) back and forth ions (BAFIONS), (b) pocket motion (PIONS), and (c) filamentary motion (FIONS).

of the first jump is distributed. All these features suggest that the ion dynamics is, by essence, heterogeneous, and this furthermore illustrates that particles that have managed to make a jump, i.e. BAFIONS AND FIONS, will likely proceed to make additional jumps. Obviously, such ion categories depend on the considered time interval, and the present characterization has a meaning only on the considered 10 ps range. The underlying (Ge,S) network structure being almost static at 600 K, and as neither short nor intermediate range (rings) structural features evolve with time, the picture which emerges is a Li dynamics evolving in a frozen network. Over longer time periods, presumably PIONs or BAFIONs will display motions typical of FIONs, but this might occur on timescales which are beyond the computer timescales.

4.4. Ionic conductivity

The ionic conductivity (σ) as a function of temperature T can be obtained from the Nernst–Einstein equation [78]:

$$\sigma(T) = \lim_{t \rightarrow \infty} \frac{e^2}{6tVk_B T} \sum_{i,j} \left\langle [\mathbf{r}_i(t) - \mathbf{r}_i(0)] [\mathbf{r}_j(t) - \mathbf{r}_j(0)] \right\rangle \quad (9)$$

where V is the volume of the simulation box, k_B is Boltzmann’s constant, e is the elementary charge, z_i and z_j are the charges of ions i and j (taken here as $z_{Li} = +1$, $z_{Ge} = +4$ and $z_S = -2$), respectively. Here $\mathbf{r}_i(t)$ are the positions of atom i , and the brackets $\langle \rangle$ denote ensemble averages.

First, we note that cross (distinct) correlations between the motions of the different atoms ($i \neq j$) are negligible compared to self contributions so that only diagonal contributions ($i = j$) from Li, Ge and S prevail. Results for the three temperatures are given in figure 11 that display calculated values in the

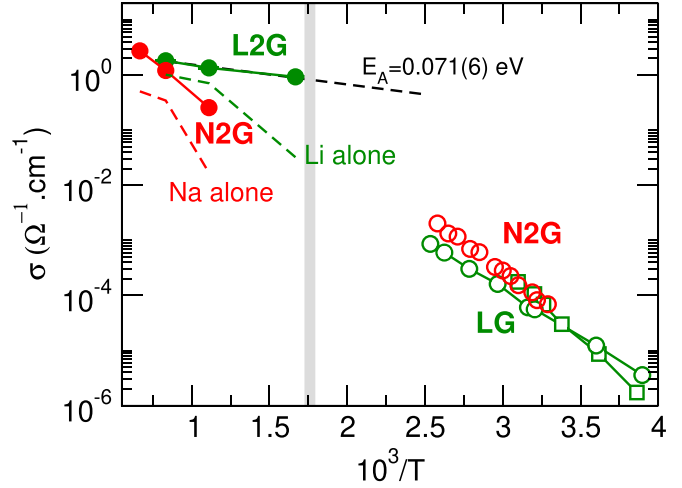


Figure 11. Calculated conductivities of L2G supercooled liquids (filled green circles), compared to the N2G analog (filled red circles [38]), and to experimental data of N2G [38] and LG glasses [20, 22]. The gray zone corresponds to the glass transition region of LG glasses (568 K [82] or 583 K [19]). The corresponding data for N2G is $T_g = 551$ K [19]. Broken colored lines correspond to the conductivity contribution of the alkali ions alone (see text for details). An Arrhenius fit to the numerical L2G data is also provided, and leads to $E_A = 0.071(6)$ eV.

supercooled state (1200 K, 900 K and 600 K) which are compared to experimental data obtained for the LG glasses [19, 20, 22]. These highlight the fact the calculated values lead to $\sigma_{Li} > \sigma_{Na}$ at fixed temperature, and are fully compatible with the data determined experimentally, and one expects to see a slightly larger conductivity in L2G glasses as compared to the reported values for the LG system [20, 22]. A crude estimate of the Arrhenius activation energy for L2G leads to $E_A = 0.071(6)$ eV (figure 11), whereas it is found $E_A = 0.436$ eV for the N2G liquid. This difference in behavior between the Na and the Li systems essentially arises from the network species contribution (Ge,S) to the conductivity, as already noticeable from the reduced temperature dependence of their diffusivity (figure 8). By focusing only on the ion contribution σ_k ($k = \text{Li, Na}$), i.e.:

$$\sigma_k = \frac{e^2}{Vk_B T} D_k(T) \quad (10)$$

one realizes that the temperature behavior of this ion contribution σ_{Li} and σ_{Na} is similar (colored broken curves in figure 11). Thus, in the liquid state, the network structure of L2G appears to play a crucial role in the temperature dependence of the conductivity, and we identify the increased polymerized network (with Q^2 species and ring structure) of L2G as the origin of this difference when compared to the sodium counterpart.

An inspection of figure 11 representing the liquid and glass data, furthermore, signals that a possible jump $\Delta\sigma$ in conductivity might appear in the glass transition region (determined in the region 568–583 K [19, 82]). This is in line with reported Arrhenius cross-overs in glassy electrolytes which manifest by a change in slope across the glass transition region

(here gray zone in figure 11), the sudden conductivity increase [83–86] being induced by the underlying network softening across T_g . This softening leads in certain electrolytes to conductivity jumps of about $\Delta\sigma \simeq 10^3\text{--}10^4 \Omega^{-1}\text{cm}^{-1}$ as in borosilicates [85] or binary CaO–SiO₂ [87]. Here, and in contrast with oxide glasses, given the already large conductivities observed in the glassy state ($>10^{-4} \Omega^{-1}\text{cm}^{-1}$), such conductivity jump might be rather small ($\Delta\sigma \simeq 10 \Omega^{-1}\text{cm}^{-1}$), as anticipated from figure 11.

5. Conclusion

Here, we have investigated from density function theory based MD the structural, dynamic and electric properties of amorphous and liquid GeS₂–2Li₂S (L2G) which has been recognized as an interesting electrolyte material because rather large conductivities can be obtained (about $10^{-4}\text{--}10^{-3} \Omega^{-1}\text{cm}^{-1}$), and used in future all-solid-state battery applications. After the seminal contributions of Ribes and co-workers [19, 20] in the mid 1980's, such glasses have received renewed interest [29–31, 82] so that contributions from numerical simulations are now timely as they can provide a detailed description of the atomic structure, prior to the establishment of structure-property relationships. These might help in investigating more complex materials [88] such as Li₁₀GeP₂S₁₂ which uses a combination of GeS₂ and P₂S₅ networks.

The present study suggests that unlike Na thiogermanates [38], L2G glasses retain a certain degree of network medium-range ordering which manifests by the presence of ring-structures including edge-sharing tetrahedral motifs that can be produced from the growing presence of Q^2 units having two bridging-sulfur (BS) atoms able to ensure the (Ge,S) network connectivity. The SRO is made of GeS_{4/2} tetrahedra with BS to non-bridging (NBS) sulfur-germanium distances which differ, and the corresponding Q^n population is determined. Features typical of Ge chalcogenides are also found such as the presence of homopolar Ge–Ge bonds which lead to anionic clusters (Ge₂S₆^{6⊖}). Calculation of the coordination numbers lead to expected results for the network species, i.e. $r_{Ge} = 4$, and $r_S = 2$, whereas the coordination of Li is found to be of about 3.5 in a defect octahedral geometry as evidenced from the S–Li–S BAD that shows specific angular contributions at 90° and 160°–180°. The tetrahedral character of Ge atoms remains unchanged with a Q^n speciation that can be defined, similarly to modified silicates or thiosilicates. As the SRO evolves from a Q^4 -based network (GeS₂) to a nearly Q^0 network (isolated molecules), the connection between the Ge tetrahedra is substantially modified with a reduction of ES elements and the presence of some dimer CS fragments (Q^1 – Q^1 connection).

Diffusivity and conductivity results suggest that L2G liquids display an increased motion with respect to the sodium counterpart. With temperature, conductivities might follow an Arrhenius behavior and are compatible with the conductivities measured in the glassy state. A detailed analysis of the atomic motion indicates that over the simulated trajectory (10–15 ps)

the Li dynamics performs in a rather complex fashion with spatially reduced motions (motion in traps leading to so-called pocket ions, PIONS) or, alternatively, long-range motions that are either of filamentary nature (FIONS) or driven by transition pathways between two cages, in some sort of back and forth motion (BAFIONS). Taken together, these results appear now helpful in decoding the properties of other sulfur-based glassy electrolytes, and might also help to understand more complex glassy systems using mixed network formers or modifiers, such as, e.g. Li₂S–GeS₂–P₂S₅ or Li₂S–Na₂S–GeS₂.

Data availability statement

The data cannot be made publicly available upon publication because no suitable repository exists for hosting data in this field of study. The data that support the findings of this study are available upon reasonable request from the authors.

Acknowledgments

The author acknowledges support from Chaire d'Excellence Sorbonne Université—Universidad Autónoma de Mexico, and from Fondation MAIF pour la recherche. Shared x-ray scattering data from Professor Keiji Itoh (University of Okayama, Japan) are gratefully acknowledged, as well as supercomputing access to the cluster Romeo from Université de Reims Champagne-Ardennes. The author has abandoned the idea of being funded by the controversial ANR. Interactions and discussions with Louis-Martin Poitras, Andrea Piarristeguy, Gerardo Naumis, Hugo Flores-Ruiz and Annie Pradel are also acknowledged.

ORCID iD

Matthieu Micoulaut  <https://orcid.org/0000-0002-0273-0563>

References

- [1] Weiss M *et al* 2021 *Adv. Energy Mater.* **11** 2101126
- [2] Tarascon J-M and Armand M 2001 *Nature* **414** 359–67
- [3] Masquelier C 2011 *Nat. Mater.* **10** 649–50
- [4] Grady Z A, Wilkinson C J, Randall C A and Mauro J C 2020 *Front. Energy Res.* **8** 218
- [5] Kennedy J 1989 *Mater. Chem. Phys.* **23** 29–50
- [6] Eckert H, Zhang Z and Kennedy J H 1990 *Chem. Mater.* **2** 273–9
- [7] Mizuno F, Hayashi A, Tadanaga K and Tatsumisago M 2005 *Adv. Mater.* **17** 918–21
- [8] Mori K, Ichida T, Iwase K, Otomo T, Kohara S, Arai H, Uchimoto Y, Ogumi Z, Onodera Y and Fukunaga T 2013 *Chem. Phys. Lett.* **584** 113–8
- [9] Ohara K *et al* 2016 *Sci. Rep.* **6** 1–9
- [10] Smith W H, Vaselabadi S A and Wolden C A 2023 *Mater. Today Commun.* **35** 105574
- [11] Mori K, Iwase K, Oba Y, Ikeda K, Otomo T and Fukunaga T 2020 *Solid State Ion.* **344** 115141
- [12] Pradel A and Piarristeguy A 2022 *C. R. Géosci.* **354** 79–99

- [13] Foix D, Martinez H, Pradel A, Ribes M and Gonbeau D 2006 *Chem. Phys.* **323** 606–16
- [14] Hayashi A, Hama S, Morimoto H, Tatsumisago M and Minami T 2001 *J. Am. Ceram. Soc.* **84** 477–79
- [15] Peng H, Ma X, Fan Z and Liang Y 2006 *J.-Chin. Ceram. Soc.* **34** 1270
- [16] Pradel A and Ribes M 1986 *Solid State Ion.* **18** 351–5
- [17] Eckert H, Kennedy J H, Pradel A and Ribes M 1989 *J. Non-Cryst. Solids* **113** 287–93
- [18] Kondo S, Takada K and Yamamura Y 1992 *Solid State Ion.* **53** 1183–6
- [19] Souquet J, Robinel E, Barrau B and Ribes M 1981 *Solid State Ion.* **3** 317–21
- [20] Ribes M, Barrau B and Souquet J 1980 *J. Non-Cryst. Solids* **38** 271–6
- [21] Senegas J and Olivier-Fourcade J 1983 *J. Phys. Chem. Solids* **44** 1033–8
- [22] Pradel A, Pagnier T and Ribes M 1985 *Solid State Ion.* **17** 147–54
- [23] Pradel A, Kuwata N and Ribes M 2003 *J. Phys.: Condens. Matter* **15** S1561
- [24] Pradel A, Rau C, Bittencourt D, Armand P, Philippot E and Ribes M 1998 *Chem. Mater.* **10** 2162–6
- [25] Kim Y, Saienga J and Martin S W 2006 *J. Phys. Chem. B* **110** 16318–25
- [26] Trevey J E, Jung Y S and Lee S-H 2011 *Electrochim. Acta* **56** 4243–7
- [27] Mori K, Kasai T, Iwase K, Fujisaki F, Onodera Y and Fukunaga T 2017 *Solid State Ion.* **301** 163–9
- [28] Itoh K, Sonobe M, Mori K, Sugiyama M and Fukunaga T 2006 *Physica B* **385** 520–2
- [29] Itoh K 2022 *Solid State Ion.* **383** 115986
- [30] Furuta K, Mori K, Onodera Y and Fukunaga T 2015 Local structure of lithium ion conducting germanium sulfide glass:(Li₂S)₄₀(GeS₂)₆₀ *Proc. 2nd Int. Symp. on Science at J-PARC-Unlocking the Mysteries of Life, Matter and the Universe* p 031004
- [31] Itoh K, Sonobe M, Sugiyama M, Mori K and Fukunaga T 2008 *J. Non-Cryst. Solids* **354** 150–4
- [32] Henderson G S 2005 *Can. Mineral.* **43** 1921–58
- [33] Micoulaut M 2008 *Am. Mineral.* **93** 1732–48
- [34] Zeidler A, Drewitt J, Salmon P, Barnes A, Crichton W, Klotz S, Fischer H, Benmore C, Ramos S and Hannon A 2009 *J. Phys.: Condens. Matter* **21** 474217
- [35] Chakraborty S, Boolchand P and Micoulaut M 2017 *Phys. Rev. B* **96** 094205
- [36] Henderson G, Soltay L and Wang H 2010 *J. Non-Cryst. Solids* **356** 2480–5
- [37] Mysen B and Richet P 2018 *Silicate Glasses and Melts* (Elsevier)
- [38] Micoulaut M, Piarristeguy A, Masson O, Escalier R, Poitras L M, Kachmar A and Pradel A 2023 *Phys. Rev. B* **108** 144205
- [39] Mauro J C and Varshneya A K 2006 *J. Am. Ceram. Soc.* **89** 2323–6
- [40] Massobrio C, Bouzid A, Boero M, Ori G, Martin E and Le Roux S 2019 *J. Phys. D: Appl. Phys.* **53** 033002
- [41] Salmon P S 2007 *J. Non-Cryst. Solids* **353** 2959–74
- [42] Polidori A, Zeidler A and Salmon P S 2020 *J. Chem. Phys.* **153** 154507
- [43] Petri I and Salmon P 2001 *J. Non-Cryst. Solids* **293** 169–74
- [44] Bauchy M and Micoulaut M 2013 *J. Non-Cryst. Solids* **377** 34–38
- [45] Bychkov E 2000 *Solid State Ion.* **136** 1111–8
- [46] Alekseev I, Fontanari D, Sokolov A, Bokova M, Kassem M and Bychkov E 2020 *Ionic Conductivity and Tracer Diffusion in Glassy Chalcogenides* vol 1 (World Scientific)
- [47] Thomas M, Peterson N L and Hutchinson E 1985 *J. Am. Ceram. Soc.* **68** 99–104
- [48] Car R and Parrinello M 1985 *Phys. Rev. Lett.* **55** 2471
- [49] Hutter J 2012 *Wiley Interdiscip. Rev.-Comput. Mol. Sci.* **2** 604–12
- [50] Perdew J P, Burke K and Ernzerhof M 1996 *Phys. Rev. Lett.* **77** 3865
- [51] Micoulaut M 2019 *J. Phys.: Condens. Matter* **31** 285402
- [52] Micoulaut M 2004 *J. Phys.: Condens. Matter* **16** L131
- [53] Micoulaut M, Pethes I, Jóvári P, Pusztai L, Krbal M, Wágner T, Prokop V, Michalík Š, Ikeda K and Kaban I 2022 *Phys. Rev. B* **106** 014206
- [54] Salmon P S 1994 *Proc. R. Soc. A* **445** 351–65
- [55] Massobrio C, Micoulaut M and Salmon P S 2010 *Solid State Sci.* **12** 199–203
- [56] Zintl E, Harder A and Dauth B 1934 *Z. Elektrochem. Angew. Phys. Chem.* **40** 588–93
- [57] Poitras L-M and Micoulaut M 2023 *Phys. Rev. B* **107** 214205
- [58] Pant A 1968 *Acta Crystallogr. B* **24** 1077–83
- [59] McDonald W T and Cruickshank D 1967 *Acta Crystallogr.* **22** 37–43
- [60] Yuan X and Cormack A N 2001 *J. Non-Cryst. Solids* **283** 69–87
- [61] Du J and Cormack A 2004 *J. Non-Cryst. Solids* **349** 66–79
- [62] Du J and Corrales L R 2006 *J. Chem. Phys.* **125** 114702
- [63] Philippot E, Ribes M and Lindqvist O 1971 *Rev. Chim. Miner.* **8** 477–89
- [64] Pauling L 1992 *J. Chem. Educ.* **69** 519
- [65] Lee J, Pradel A, Taillades G, Ribes M and Elliott S 1997 *Phys. Rev. B* **56** 10934
- [66] Price D L and Ellison A J 1994 *J. Non-Cryst. Solids* **177** 293–8
- [67] Eckert H, Zhang Z and Kennedy J H 1989 *J. Non-Cryst. Solids* **107** 271–82
- [68] Pradel A, Taillades G, Ribes M and Eckert H 1995 *J. Non-Cryst. Solids* **188** 75–86
- [69] Micoulaut M and Kerner R 1997 *J. Phys.: Condens. Matter* **9** 2551
- [70] Seo I 2009 *PhD Thesis* Iowa State University
- [71] Olivier-Fourcade J, Jumas J, Ribes M, Philippot E and Maurin M 1978 *J. Solid State Chem.* **23** 155–76
- [72] Maekawa H, Maekawa T, Kawamura K and Yokokawa T 1991 *J. Non-Cryst. Solids* **127** 53–64
- [73] Tokuda Y, Uchino T and Yoko T 2001 *J. Non-Cryst. Solids* **282** 256–64
- [74] Le Roux S and Jund P 2010 *Comput. Mater. Sci.* **49** 70–83
- [75] King S V 1967 *Nature* **213** 1112–3
- [76] Franzblau D 1991 *Phys. Rev. B* **44** 4925
- [77] Micoulaut M 2016 *Rep. Prog. Phys.* **79** 066504
- [78] Hansen J P and McDonald I R 2013 *Theory of Simple Liquids: With Applications to Soft Matter* (Academic)
- [79] Kob W, Donati C, Plimpton S J, Poole P H and Glotzer S C 1997 *Phys. Rev. Lett.* **79** 2827
- [80] Chaudhuri P, Berthier L and Kob W 2007 *Phys. Rev. Lett.* **99** 060604
- [81] Appignanesi G, Fris J R, Montani R and Kob W 2006 *Phys. Rev. Lett.* **96** 057801
- [82] Kim Y, Saienga J and Martin S W 2005 *J. Non-Cryst. Solids* **351** 3716–24
- [83] Golodnitsky D, Strauss E, Peled E and Greenbaum S 2015 *J. Electrochem. Soc.* **162** A2551
- [84] Tu C-H, Veith L, Butt H-J and Floudas G 2022 *Macromolecules* **55** 1332–41
- [85] Malki M, Magnien V, Pinet O and Richet P 2015 *Geochim. Cosmochim. Acta* **165** 137–47
- [86] Fan H, Del Campo L, Montouillout V and Malki M 2020 *J. Non-Cryst. Solids* **543** 120160
- [87] Malki M and Echegut P 2003 *J. Non-Cryst. Solids* **323** 131–6
- [88] Kamaya N *et al* 2011 *Nat. Mater.* **10** 682–6